Cite as: The LHAASO Collaboration, *Science* 10.1126/science.abg5137 (2021).

# PeV gamma-ray emission from the Crab Nebula

**The LHAASO Collaboration*†**

*Corresponding authors: Zhen Cao (caozh@ihep.ac.cn); S. Z. Chen (chensz@ihep.ac.cn); S. J. Lin (linsj6@mail.sysu.edu.cn); S. S. Zhang (zhangss@ihep.ac.cn); M. Zha (zham@ihep.ac.cn); Cong Li (licong@ihep.ac.cn); L. Y. Wang (wangly@ihep.ac.cn); L. Q. Yin (yinlq@ihep.ac.cn); F. Aharonian (felix.aharonian@mpi-hd.mpg.de); R. Y. Liu (ryliu@nju.edu.cn)

†The LHAASO Collaboration authors and affiliations are listed in the supplementary materials.

**The Crab Nebula is a bright source of gamma-rays powered by the Crab Pulsar's rotational energy, through the formation and termination of a relativistic electron-positron wind. We report the detection of γ-rays from this source with energies from $5 \times 10^{-4}$ to 1.1 petaelectronvolts (PeV), with a spectrum showing gradual steepening over three energy decades. The ultra-high-energy photons imply the presence of a PeV electron accelerator (a pevatron) in the nebula, with an acceleration rate exceeding 15% of the theoretical limit. We constrain the pevatron's size between 0.025 and 0.1 pc, and magnetic field ≈110 μG. The production rate of PeV electrons, $2.5 \times 10^{36}$ erg $s^{-1}$, constitutes 0.5% of the pulsar spin-down luminosity, although we cannot exclude a contribution of PeV protons to the production of the highest energy γ-rays.**

The Crab Nebula is a remnant of the explosion of a massive star. The nebula formed on 1054 August 24, being recorded in Chinese chronicles as a 'guest star' (*1*). It is the brightest known pulsar wind nebula, an extended nonthermal structure powered by the ultrarelativistic electron-positron wind from the central neutron star (the Crab Pulsar). This makes the Crab Nebula one of the brightest γ-ray sources in the sky, which has been observed for decades at TeV energies (*2*). At the transition from GeV to TeV energies, the spectral energy distribution (SED; $E^2 dN / dE$, where $dN / dE$ is the differential flux of radiation at the photon energy $E$) reaches a maximum around 100 GeV (*3*, *4*). Previous observations reported a detection at ≈80 TeV (*5*), and measured the spectrum up to 300 TeV (*6*–*8*). The angular size of the γ-ray source at TeV energies has been reported ≈50 arcsec (*9*). The Crab Nebula was among the sources detected at energies above 100 TeV using the Large High Altitude Air Shower Observatory (LHAASO) (*10*).

LHAASO is a dual-purpose complex of particle detectors, designed for the study of cosmic rays (CRs) and γ-rays in the sub-TeV to 1000 PeV energy range (*11*, *12*). When a very high energy extraterrestrial particle enters Earth's atmosphere, it initiates a cascade consisting of secondary hadrons, leptons, and photons, known as an air shower. The LHAASO detectors record different components of these air showers, which are used to reconstruct the type, energy and arrival direction of the primary particles.

LHAASO consists of three arrays (*13*). The largest is the square kilometer array (KM2A) comprising surface counters and subsurface muon detectors. KM2A is designed to detect cosmic rays (CR) from 10 TeV to 100 PeV and distinguish γ-ray photons from CRs using the muon detector array. The muon content in an air shower event can be used to effectively reject hadronic showers, which are initiated by CRs. The surface array of KM2A is used to determine the energy and arrival direction of the primary particles. KM2A operates as an Ultra High Energy (UHE, $E_\gamma > 0.1$ PeV) γ-ray telescope (*14*) with energy resolution of ≤20% and angular resolution of 0.25°. For γ-rays above 50 TeV, the sensitivity of KM2A reaches the flux level of $10^{-14}$ erg $cm^{-2} s^{-1}$ for a point source like the Crab Nebula in one year of observations (*12*).

The Water Cherenkov Detector Array (WCDA) consists of three ponds with total area of 0.08 $km^2$, sensitive to γ-rays down to 0.1 TeV with an angular resolution $\delta\psi \approx 0.2°$ (*15*). WCDA is designed to perform deep surveys of very high energy γ-ray sources, including the Crab Nebula for both pulsed and unpulsed signals. The sensitivity at energies above 2 TeV reaches the flux level of $10^{-12}$ erg $cm^{-2} s^{-1}$ for a point source like the Crab Nebula in one year of observations (*12*). At energies above 0.1 PeV, WCDA also serves as an additional muon detector to enhance the determination between electromagnetic and hadronic showers detected by KM2A.

KM2A and WCDA are complemented by the Wide-Field-of-view Cherenkov Telescope Array (WFCTA) (*16*), designed to consist of 18 telescopes (of which 14 have been constructed) that detect Cherenkov radiation emitted by air showers induced by CRs, with energy ranging from 0.1 to 1000 PeV. Cherenkov light in showers initiated by γ-rays at energies above 0.1 PeV is recorded by WFCTA telescopes which cover a 32° × 112° region of the northern sky, through which the Crab Nebula passes every day.

## LHAASO Observations of the Crab Nebula

On 2020 January 11 at 17:59:18 Coordinated Universal Time (UTC), a giant air shower was recorded by all three LHAASO detectors. The shower arrived from the direction of the Crab Nebula and was centered in the western part of KM2A (Fig. 1A). WCDA was also triggered, despite being 150 m away from the shower core. The event occurred after local midnight, when eight WFCTA telescopes were operational. The Cherenkov radiation from the air shower appeared in the Field of View (FoV) of Telescope No.10 and triggered it (Fig. 1C).

We identify the event as a $\gamma$-ray induced shower, based on 4996 particles (electrons, photons, muons, hadrons) recorded by 395 surface detectors, and 15 muons recorded by 11 underground detectors of KM2A. The probability for this event to be a misidentified CR is estimated as 0.1% (*13*). Two independent estimates of the shower energy were derived from the KM2A and WFCTA data: 0.88 ± 0.11 PeV and $0.92^{+0.28}_{-0.20}$ PeV, respectively. The former value has previously been reported as the maximum energy of $\gamma$-rays detected from the Crab Nebula by LHAASO (*10*).

Approximately one year later, 2021 January 4 at 16:45:06 UTC, another shower was registered by KM2A at even higher energy, 1.12 ± 0.09 PeV. This event occurred at zenith angle 12.9°, closer to vertical and therefore better measured by KM2A than the previous shower. Unfortunately, the primary photon arrived one hour before the Crab entered the FoV of the WFCTA telescopes. While the number of detected secondary particles (5094) exceeded those in the previous event, the number of muons (14) was fewer, so we also identified this event as a $\gamma$-ray induced shower with a misidentification probability of 0.03%.

KM2A operated for 314 days at half of its design capacity and a further 87 days at three quarters of its design capacity. In that time, a total of 89 UHE $\gamma$-rays with energy exceeding 0.1 PeV were detected from the Crab. Figure 2 shows the integrated $\gamma$-ray detection rate, re-normalized to the nominal 1 km$^2$ array and one hour exposure time, assuming the Crab is within the FoV of KM2A (approximately 7.4 hours per day with zenith angle less than 50°). Above 0.1 PeV, we find about 0.05 events per hour, equivalent to 135 events per year. Figure 2 also shows the detection rate of the CR-induced showers within a cone of 1° centered on the Crab, both before and after applying the CR shower rejection based on the muon content in the showers. This 'muon cut' filter requires that the number of muons detected by KM2A in the shower must be less than 1/230 of the number of particles detected by the KM2A surface counters. The cut reduces the cosmic ray background by factors of 1,000 and 500,000 at 50 TeV and 1 PeV, respectively. At energies above 0.1 PeV, the detection rate of $\gamma$-rays from the Crab exceeds the CR induced background by an order of magnitude. Because the Point Spread Function (PSF) of KM2A is $\delta\psi \approx 0.25°$, the CR background could be lower by an additional factor of $(1° / \delta\psi)^2 \approx 16$.

## Spectral Energy Distribution

The $\gamma$-ray fluxes in the energy range from 0.5 TeV to 13 TeV were measured using the WCDA pond. From 2019 September to 2020 October, the total exposure was 343.5 transits of the Crab Nebula. The KM2A measurements in the observation period reported above cover the higher energy range from 10 TeV to 1.6 PeV. We combined the WCDA and KM2A data to determine the SED of the Crab Nebula, shown in Fig. 3A. The two independent measurements are consistent with a simple SED functional form

$$\mathrm{d}N/\mathrm{d}E = (8.2 \pm 0.2) \times 10^{-14} \left(E/10\ \mathrm{TeV}\right)^{-\Gamma}\ \mathrm{cm}^{-2}\ \mathrm{s}^{-1}\ \mathrm{TeV}^{-1},$$

where $N$ is the number of $\gamma$-rays, $E$ is the $\gamma$-ray energy and $\Gamma$ is the energy dependent spectral index. The two measurements are connect smoothly in the small overlapping region around 12.5 TeV. In this energy bin, the discrepancy between flux measured by KM2A and WCDA is 1.3$\sigma$. The overall $\chi^2$ / *dof* is 9.3/14, where *dof* is the number of degrees of freedom. No systematic deviation between the two segments of the SED is found. The functional form of the spectral index, $\Gamma = (2.90 \pm 0.01) + (0.19 \pm 0.02) \log_{10}(E/10\ \mathrm{TeV})$, implies a gradual steepening of the spectrum characterized by the local index $\Gamma$, from ≈2.5 at 1 TeV to 3.7 at 1 PeV (Fig. 3B).

Figure 3A also shows previous measurements using atmospheric Cherenkov telescopes (*5*, *6*, *17*, *18*) and air shower arrays (*7*, *8*, *19*). These are consistent with the WCDA and KM2A data from sub-TeV to multi-TeV energies, including the flux at the highest energy previously reported, $E_\gamma \approx 300$ TeV (*8*).

## Origin of the PeV photons and electrons

Photons from the Crab Nebula have been detected over 22 decades of energy, from MHz radio to UHE $\gamma$-rays, in both pulsed and unpulsed components. $\gamma$-rays can be produced in three physically distinct sites - in the pulsar's magnetosphere, the ultrarelativistic electron-positron (hereafter, simply electron) wind, and in the nebula. UHE $\gamma$-rays are absorbed in the strong magnetic field of the pulsar, so a pulsed $\gamma$-ray component from the magnetosphere has been predicted only in energy range of MeV-to-GeV. However, a previous detection of pulsed TeV $\gamma$-rays from the Crab (*20*) indicates pulsed $\gamma$-ray emission occurs in the wind (*21–23*). Extension of this component to UHE $\gamma$-rays is theoretically unexpected. We nevertheless searched for a pulsed component in the LHAASO data, but did not detect one, limited by the photon statistics. We therefore assume that the entire flux detected by LHAASO consists of an unpulsed component that is produced in the nebula.

The broad-band non-thermal emission of the Crab Nebula is dominated by two mechanisms - synchrotron radiation and

inverse Compton (IC) scattering of relativistic electrons interacting with the ambient magnetic and radiation fields (*24*, *25*). In the standard paradigm, the acceleration of electrons is initiated by the termination of the wind, at a standing reverse shock located a distance $R \approx 0.1$ parsec (pc) from the pulsar (*26*, *27*). Although the details of the acceleration mechanism remain unknown, the detection of PeV photons allows us to estimate the accelerator size $l$, the magnetic field strength $B$, and the minimum acceleration rate $\eta$.

In the Crab Nebula, several radiation fields supply target photons for the IC scattering of electrons. However, at energies above 100 TeV, the 2.7 K cosmic microwave background radiation (CMBR) dominates the $\gamma$-ray production (*25*, *28*). Because the CMBR is well quantified, the $\gamma$-ray data provides direct information about the parent electrons. $\gamma$-ray production above 100 TeV proceeds in the Klein-Nishina regime, where the energies of the upscattered photon $E_\gamma$ and the parent electron $E_e$ are linked through the simple relation $E_\gamma = 0.37\left(E_e/1\ \mathrm{PeV}\right)^{1.3}\ \mathrm{PeV}$, which over two energy decades, from 30 TeV to 3 PeV, is accurate to within 10% (see fig. S7), or equivalently

$$E_e \simeq 2.15\left(E_\gamma/1\ \mathrm{PeV}\right)^{0.77}\ \mathrm{PeV} \quad (1)$$

Thus, for the 1.1 PeV photon, the energy of the parent electron is 2.3 PeV. Correspondingly, the mean energies of the synchrotron $\left(\varepsilon_{\mathrm{syn}}\right)$ and IC $\left(E_\gamma\right)$ photons produced by the same electron in the ambient magnetic field $B$, are related by

$$\varepsilon_{\mathrm{syn}} = 9.3\left(E_\gamma/1\ \mathrm{PeV}\right)^{1.5}\left(B/100\ \mu\mathrm{G}\right)\ \mathrm{MeV} \quad (2)$$

Simultaneous modelling (*13*) of the synchrotron and IC components constrains the magnetic field strength within a narrow interval, $B \simeq 112^{+15}_{-13}\ \mu\mathrm{G}$ (see Fig. 4 and discussion below). The upper limit is set by the requirement for the synchrotron radiation of the same electrons responsible for the production of 1 PeV photons to not overshoot the measured MeV flux (*29*). The lower limit is set by requiring the electron energy $E_e$ and the accelerator's linear size, $l$, to meet the condition that the electron gyroradius $R_g = E_e/eB$ ($e$ is the charge of electron) cannot exceed $l$. Using Eq. 1, we find

$$\left(B/100\ \mu\mathrm{G}\right)\left(l/1\ \mathrm{pc}\right) \geq 0.023\left(E_\gamma/1\ \mathrm{PeV}\right)^{0.77} \quad (3)$$

Magnetohydrodynamic (MHD) models of the Crab Nebula (*26*, *27*) postulate that electrons are accelerated at the termination of an electron wind, then advected into the nebula through the MHD outflow. X-ray imaging of the inner parts of the nebula (*30*) indicates that the acceleration site is located close to the termination shock, at $R \approx 0.1$ – 0.14 pc from the pulsar (*28*). The linear size of the accelerator must exceed the gyroradius, $l \geq R$; this imposes a lower limit on the magnetic field from Eq. 3, $B \geq 20\ \mu\mathrm{G}$. On the other hand, the standard one-zone model, which assumes that both the synchrotron and IC radiation components are produced in the same region by the same electron population, gives $B \simeq 112\ \mu\mathrm{G}$ (see Fig. 4). Then, from Eq. 3 we find that $l \geq 0.02$ pc. These constraints are inconsistent with estimates of the characteristic size and magnetic field in the region(s) where the flares of the MeV/GeV $\gamma$-ray emission ("Crab flares") (*31*) originate. Those variations of $\gamma$-ray fluxes on timescales of days are interpreted as fast acceleration and synchrotron cooling of PeV electrons in compact ($R \leq 0.01$ pc) highly magnetized ($B \geq 1$ mG) regions (see (*32*) for a review). In the presence of such a large magnetic field, the IC $\gamma$-ray component is suppressed; however this does not exclude an indirect link between the PeV electrons responsible for the UHE $\gamma$-ray emission and the synchrotron MeV/GeV flares.

The detection of ~1 PeV photons implies an acceleration rate which overcomes the synchrotron losses of the parent electrons up to PeV energies. The acceleration rate of electrons is $\dot{E} = e\mathcal{E}c = \eta eBc$, where $\eta$ is the ratio of the projection of the electric field $\mathcal{E}$, averaged over the particle trajectory, to the magnetic field, $\eta = \mathcal{E}/B$. This parameter characterizes the acceleration efficiency and is always smaller than 1; in objects where $\eta \to 1$, the accelerator proceeds at the maximum rate allowed by classical electrodynamics and ideal MHD (*33*). The maximum energy of electrons then is determined by the balance between the acceleration and the energy loss rates: $E_{e,\max} \approx 5.8\eta^{1/2}\left(B/100\ \mu\mathrm{G}\right)^{-1/2}$ PeV. Using the relation between $E_\gamma$ and $E_e$ given by Eq. 1, we find

$$\eta = 0.14\left(B/100\ \mu\mathrm{G}\right)\left(E_\gamma/1\ \mathrm{PeV}\right)^{1.54}\ \mathrm{PeV} \quad (4)$$

Thus, for the detected $E_\gamma = 1.1$ PeV and the magnetic field $B \simeq 112\ \mu\mathrm{G}$ derived from the one-zone model (Fig. 4), we find that the acceleration proceeds at the rate $\eta \approx 0.16$. For comparison, at the diffusive shock acceleration in young supernova remnants (*34*), $\eta$ is smaller by at least 3 orders of magnitude.

For the distance to the Crab Nebula, $d \approx 2$ kpc (*35*), the luminosity in PeV $\gamma$-rays is estimated as $L_{\gamma,\mathrm{PeV}} = 4\pi d^2 F_\gamma \approx 5\times10^{31}\ \mathrm{erg\ s^{-1}}$, where $F_\gamma \approx 10^{-13}\ \mathrm{erg\ s^{-1}}$ is the energy flux of 0.5 to 1.1 PeV $\gamma$-rays (Fig. 4). In the Klein-Nishina limit, the IC cooling time of electrons in 2.7 K CMBR is $t_{\mathrm{IC}} \simeq 5\times10^{11}\left(E_e/1\ \mathrm{PeV}\right)^{0.7}$ s (*36*) or, for the given $E_\gamma$, using Eq. 1 we have $t_{\mathrm{IC}} \simeq 8\times10^{11}\left(E_\gamma/1\ \mathrm{PeV}\right)^{0.54}$ s. Thus, the total energy held by the ≥1 PeV electrons responsible for production of ≥0.5 PeV $\gamma$-rays is estimated as $W_{e,\mathrm{PeV}} = L_{\gamma,\mathrm{PeV}} t_{\mathrm{IC}} \approx 4\times10^{43}$ erg. Because the overall cooling of PeV electrons is dominated by synchrotron losses $\left(t_{\mathrm{syn}} \ll t_{\mathrm{IC}}\right)$, the injection rate of PeV electrons

$\dot{W}_{\rm e,PeV} = W_{\rm e,PeV}/t_{\rm syn} \approx 2\times10^{36}\left(B/100\ \mu{\rm G}\right)^2$ erg s$^{-1}$. Thus, within the framework of the standard one-zone model with $B$ =112 μG, the acceleration power of PeV electrons constitutes ≈0.5% fraction of the pulsar's spin-down luminosity, $L_{\rm SD} \approx 5\times10^{38}$ erg s$^{-1}$ (*27*).

**Multi-wavelength Modeling**

We consider whether the detection of PeV photons agrees with predictions from the standard MHD paradigm of the Crab Nebula, which assumes that nonthermal emission from X-rays to multi-TeV γ-rays is produced by electrons accelerated at the termination of the pulsar wind (*25*, *28*, *37–39*). We modeled the Crab's multi-wavelength radiation within the idealized Synchrotron-IC one-zone model, assuming a homogeneous spatial distribution of the magnetic field and electrons (Fig. 4). For $E_\gamma \geq 100$ TeV γ-rays the dominant target for IC scattering is the 2.7 K CMBR, with properties that are known more precisely than the targets at lower energies. For a steady-state electron energy distribution, above 1 TeV, we assumed a power-law function terminated by a super-exponential cutoff at the high-energy end. Figure 4 shows the SED model using three free parameters - the power-law slope $\alpha = 3.42$, cutoff energy $E_0 = 2.15$ PeV and magnetic field $B$ = 112 μG, which reproduces the observations from the X-rays to multi-MeV γ-rays with synchrotron radiation, and the TeV to PeV γ-rays with IC radiation. Below 1 TeV, the electron spectrum must undergo a break to avoid conflicting with the synchrotron radiation at optical to radio frequencies, and to provide a smooth transition of the IC radiation from TeV to GeV energies (*13*).

The one-zone model in Fig. 4 is tightly constrained; the 3-sigma limits on the index α (3.37 to 3.47) are constrained by the uncertainty of the X-ray data. Because ≥ 10 TeV electrons are cooled on short timescales, the index of the initial (acceleration) spectrum must be close to 2.4. The magnetic field is determined by the flux ratio of the synchrotron and IC components, with 3 sigma range from 100 to 130 μG. For these values of α and $B$, the cutoff energy $E_0$ is set by the synchrotron and IC spectra above 10 MeV and 100 TeV, respectively. The derived ranges of magnetic field and the power-law index of electrons are consistent with previous studies based on the Synchrotron-IC one-zone model (*28*, *39*) as well as MHD flow models (*25*, *40*, *41*) in which the magnetic field's radial distribution is determined by the wind-magnetization parameter $\sigma_B$. The magnetic field $B \simeq 112$ G derived for the production region of multi-TeV to PeV γ-rays, is a factor of 2-3 smaller than the average nebular magnetic field, consistent with the MHD flow model (*27*). The latter predicts reduced magnetic field at the termination shock for a broad range of the magnetization parameter $\sigma_B$ between 0.001 and 0.01 (*27*).

Within the one-zone model, the IC γ-ray spectrum can be precisely calculated. While the KM2A spectral points from 10 TeV to 1 PeV agree with the one-zone model within the statistical uncertainties, there are possible deviations from its predictions. Between 60 TeV and 500 TeV, the two differ with a significance of 4σ, with the observational data having a steeper spectrum than the one-zone model predictions. The possible excess around one PeV indicates an opposite tendency - a hardening of the spectrum. A hardening of the electron spectrum is difficult to accommodate theoretically with plausible assumptions. The problem of suppression of the one-zone spectrum at 1 PeV can be circumvented by introducing a second population of PeV electrons. This could also explain the inconsistency of the synchrotron part of the SED with the one-zone model (fig. S4) by decoupling the highest energy synchrotron and IC components, assuming that the MeV synchrotron radiation is predominantly produced in compact highly magnetized regions, while the PeV IC photons originate from regions with $B \leq 100$ μG. A second electron component could extend the SED to a few PeV but not much further. From Eq. 4 it follows that, even for η = 1 and minimum allowed magnetic field, $B \geq 20$ μG, then the maximum energy of photons cannot exceed 4 PeV. Any detection of γ-rays well beyond 1 PeV would require a non-leptonic origin for the extra component of radiation, e.g., multi-PeV protons and atomic nuclei in the nebula.

Because of the limited energy budget available for acceleration of protons, hadronic interactions cannot be responsible for the overall broad-band γ-ray luminosity. However, the contribution of hadronic interactions at PeV energies could be non-negligible. The γ-ray production efficiency of hadronic interactions, i.e., the fraction of the proton kinetic energy converted to γ-rays, is determined by the ratio $\kappa = t_{\rm esc} / t_{\rm pp}$, where $t_{\rm esc}$ is the confinement time of protons inside the nebula, and $t_{\rm pp} \approx 1.5 \times 10^8\ n^{-1}$ year is the cooling time of protons through the production and decay of the secondary $\pi^0$-mesons. For the average density of the nebular gas $n \approx 10$ cm$^{-3}$, the radiation efficiency is low; even for the most effective confinement of 10 PeV protons, $t_{\rm esc} \leq 250$ year (*13*), thus $\kappa \leq 5 \times 10^{-5}$. To explain the PeV γ-ray luminosity, $L_\gamma \approx 5 \times 10^{31}$ erg s$^{-1}$, the acceleration power of ~10 PeV parent protons would need to be $\dot{W}_{\rm p} = W_{\rm p}/t_{\rm esc} = \kappa^{-1} L_\gamma \approx 10^{36}$ erg s$^{-1}$ or, in the case of a broad $E^{-2}$ type proton spectrum, an order of magnitude larger. These estimates are supported by numerical calculations (fig. S5). They avoid exceeding the theoretical constraints on the proton fraction (*42*) only if there is effective proton confinement in the nebula.

**REFERENCES AND NOTES**


1. K. Lundmark, Suspected New Stars Recorded in Old Chronicles and Among Recent Meridian Observations. *Publ. Astron. Soc. Pac.* **33**, 225 (1921). doi:10.1086/123101
2. J. M. Lang *et al*., *International Cosmic Ray Conference* (1990), vol. 2 of *International*

*Cosmic Ray Conference*, p. 139.
3. M. Arakawa, M. Hayashida, D. Khangulyan, Y. Uchiyama, Detection of Small Flares from the Crab Nebula with Fermi-LAT. *Astrophys. J.* **897**, 33 (2020). doi:10.3847/1538-4357/ab9368
4. J. Aleksić, S. Ansoldi, L. A. Antonelli, P. Antoranz, A. Babic, P. Bangale, J. A. Barrio, J. Becerra González, W. Bednarek, E. Bernardini, B. Biasuzzi, A. Biland, O. Blanch, S. Bonnefoy, G. Bonnoli, F. Borracci, T. Bretz, E. Carmona, A. Carosi, P. Colin, E. Colombo, J. L. Contreras, J. Cortina, S. Covino, P. Da Vela, F. Dazzi, A. De Angelis, G. De Caneva, B. De Lotto, E. de Oña Wilhelmi, C. Delgado Mendez, M. Doert, D. Dominis Prester, D. Dorner, M. Doro, S. Einecke, D. Eisenacher, D. Elsaesser, M. V. Fonseca, L. Font, K. Frantzen, C. Fruck, D. Galindo, R. J. García López, M. Garczarczyk, D. Garrido Terrats, M. Gaug, N. Godinović, A. González Muñoz, S. R. Gozzini, D. Hadasch, Y. Hanabata, M. Hayashida, J. Herrera, D. Hildebrand, J. Hose, D. Hrupec, W. Idec, V. Kadenius, H. Kellermann, K. Kodani, Y. Konno, J. Krause, H. Kubo, J. Kushida, A. La Barbera, D. Lelas, N. Lewandowska, E. Lindfors, S. Lombardi, M. López, R. López-Coto, A. López-Oramas, E. Lorenz, I. Lozano, M. Makariev, K. Mallot, G. Maneva, N. Mankuzhiyil, K. Mannheim, L. Maraschi, B. Marcote, M. Mariotti, M. Martínez, D. Mazin, U. Menzel, J. M. Miranda, R. Mirzoyan, A. Moralejo, P. Munar-Adrover, D. Nakajima, A. Niedzwiecki, K. Nilsson, K. Nishijima, K. Noda, N. Nowak, R. Orito, A. Overkemping, S. Paiano, M. Palatiello, D. Paneque, R. Paoletti, J. M. Paredes, X. Paredes-Fortuny, M. Persic, P. G. Prada Moroni, E. Prandini, S. Preziuso, I. Puljak, R. Reinthal, W. Rhode, M. Ribó, J. Rico, J. Rodriguez Garcia, S. Rügamer, A. Saggion, T. Saito, K. Saito, K. Satalecka, V. Scalzotto, V. Scapin, C. Schultz, T. Schweizer, S. N. Shore, A. Sillanpää, J. Sitarek, I. Snidaric, D. Sobczynska, F. Spanier, V. Stamatescu, A. Stamerra, T. Steinbring, J. Storz, M. Strzys, L. Takalo, H. Takami, F. Tavecchio, P. Temnikov, T. Terzić, D. Tescaro, M. Teshima, J. Thaele, O. Tibolla, D. F. Torres, T. Toyama, A. Treves, M. Uellenbeck, P. Vogler, R. M. Wagner, R. Zanin, D. Horns, J. Martín, M. Meyer, Measurement of the Crab Nebula spectrum over three decades in energy with the MAGIC telescopes. *J. High Energy Astrophys.* **5–6**, 30–38 (2015). doi:10.1016/j.jheap.2015.01.002
5. F. Aharonian, A. Akhperjanian, M. Beilicke, K. Bernlohr, H.-G. Börst, H. Bojahr, O. Bolz, T. Coarasa, J. L. Contreras, J. Cortina, S. Denninghoff, M. V. Fonseca, M. Girma, N. Gotting, G. Heinzelmann, G. Hermann, A. Heusler, W. Hofmann, D. Horns, I. Jung, R. Kankanyan, M. Kestel, A. Kohnle, A. Konopelko, D. Kranich, H. Lampeitl, M. Lopez, E. Lorenz, F. Lucarelli, O. Mang, D. Mazin, H. Meyer, R. Mirzoyan, A. Moralejo, E. Ona-Wilhelmi, M. Panter, A. Plyasheshnikov, G. Pühlhofer, R. de los Reyes, W. Rhode, J. Ripken, G. Rowell, V. Sahakian, M. Samorski, M. Schilling, M. Siems, D. Sobzynska, W. Stamm, M. Tluczykont, V. Vitale, H. J. Völk, C. A. Wiedner, W. Wittek, The Crab Nebula and Pulsar between 500 GeV and 80 TeV: Observations with the HEGRA Stereoscopic Air Cerenkov Telescopes. *Astrophys. J.* **614**, 897 (2004). doi:10.1086/423931
6. MAGIC Collaboration, MAGIC very large zenith angle observations of the Crab Nebula up to 100 TeV. *Astron. Astrophys.* **635**, A158 (2020). doi:10.1051/0004-6361/201936899
7. A. U. Abeysekara, A. Albert, R. Alfaro, C. Alvarez, J. D. Álvarez, J. R. A. Camacho, R. Arceo, J. C. Arteaga-Velázquez, K. P. Arunbabu, D. A. Rojas, H. A. A. Solares, V. Baghmanyan, E. Belmont-Moreno, S. Y. BenZvi, C. Brisbois, K. S. Caballero-Mora, T. Capistrán, A. Carramiñana, S. Casanova, U. Cotti, J. Cotzomi, S. C. de León, E. D. Fuente, C. León, S. Dichiara, B. L. Dingus, M. A. DuVernois, J. C. Díaz-Vélez, R. W. Ellsworth, K. Engel, C. Espinoza, B. Fick, H. Fleischhack, N. Fraija, A. Galván-Gámez, J. A. García-González, F. Garfias, M. M. González, J. A. Goodman, J. P. Harding, S. Hernandez, J. Hinton, B. Hona, F. Hueyotl-Zahuantitla, C. M. Hui, P. Hüntemeyer, A. Iriarte, A. Jardin-Blicq, V. Joshi, S. Kaufmann, D. Kieda, A. Lara, W. H. Lee, H. L. Vargas, J. T. Linnemann, A. L. Longinotti, G. Luis-Raya, J. Lundeen, K. Malone, S. S. Marinelli, O. Martinez, I. Martinez-Castellanos, J. Martínez-Castro, H. Martínez-Huerta, J. A. Matthews, P. Miranda-Romagnoli, J. A. Morales-Soto, E. Moreno, M. Mostafá, A. Nayerhoda, L. Nellen, M. Newbold, M. U. Nisa, R. Noriega-Papaqui, A. Peisker, E. G. Pérez-Pérez, J. Pretz, Z. Ren, C. D. Rho, C. Rivière, D. Rosa-González, M. Rosenberg, E. Ruiz-Velasco, H. Salazar, F. S. Greus, A. Sandoval, M. Schneider, H. Schoorlemmer, M. S. Arroyo, G. Sinnis, A. J. Smith, R. W. Springer, P. Surajbali, E. Tabachnick, M. Tanner, O. Tibolla, K. Tollefson, I. Torres, T. Weisgarber, S. Westerhoff, J. Wood, T. Yapici, A. Zepeda, H. Zhou, Measurement of the Crab Nebula Spectrum Past 100 TeV with HAWC. *Astrophys. J.* **881**, 134 (2019). doi:10.3847/1538-4357/ab2f7d
8. M. Amenomori, Y. W. Bao, X. J. Bi, D. Chen, T. L. Chen, W. Y. Chen, X. Chen, Y. Chen, S. W. Cirennima, S. W. Cui, L. K. Danzengluobu, L. K. Ding, J. H. Fang, K. Fang, C. F. Feng, Z. Feng, Z. Y. Feng, Q. Gao, Q. B. Gou, Y. Q. Guo, H. H. He, Z. T. He, K. Hibino, N. Hotta, H. Hu, H. B. Hu, J. Huang, H. Y. Jia, L. Jiang, H. B. Jin, F. Kajino, K. Kasahara, Y. Katayose, C. Kato, S. Kato, K. Kawata, M. Kozai, G. M. Labaciren, G. M. Le, A. F. Li, H. J. Li, W. J. Li, Y. H. Lin, B. Liu, C. Liu, J. S. Liu, M. Y. Liu, Y. Q. Lou, H. Lu, X. R. Meng, H. Mitsui, K. Munakata, Y. Nakamura, H. Nanjo, M. Nishizawa, M. Ohnishi, I. Ohta, S. Ozawa, X. L. Qian, X. B. Qu, T. Saito, M. Sakata, T. K. Sako, Y. Sengoku, J. Shao, M. Shibata, A. Shiomi, H. Sugimoto, M. Takita, Y. H. Tan, N. Tateyama, S. Torii, H. Tsuchiya, S. Udo, H. Wang, H. R. Wu, L. Xue, K. Yagisawa, Y. Yamamoto, Z. Yang, A. F. Yuan, L. M. Zhai, H. M. Zhang, J. L. Zhang, X. Zhang, X. Y. Zhang, Y. Zhang, Y. Zhang, Y. Zhang, X. X. Zhaxisangzhu, X. X. Zhou; Tibet AS$_\gamma$ Collaboration, First Detection of Photons with Energy beyond 100 TeV from an Astrophysical Source. *Phys. Rev. Lett.* **123**, 051101 (2019). doi:10.1103/PhysRevLett.123.051101 Medline
9. H.E.S.S. Collaboration, Resolving the Crab pulsar wind nebula at teraelectronvolt energies. *Nat. Astron.* **4**, 167–173 (2020). doi:10.1038/s41550-019-0910-0
10. Z. Cao, F. A. Aharonian, Q. An, Axikegu, L. X. Bai, Y. X. Bai, Y. W. Bao, D. Bastieri, X. J. Bi, Y. J. Bi, H. Cai, J. T. Cai, Z. Cao, J. Chang, J. F. Chang, X. C. Chang, B. M. Chen, J. Chen, L. Chen, L. Chen, L. Chen, M. J. Chen, M. L. Chen, Q. H. Chen, S. H. Chen, S. Z. Chen, T. L. Chen, X. L. Chen, Y. Chen, N. Cheng, Y. D. Cheng, S. W. Cui, X. H. Cui, Y. D. Cui, B. Z. Dai, H. L. Dai, Z. G. Dai, Danzengluobu, D. Della Volpe, B. D Ettorre Piazzoli, X. J. Dong, J. H. Fan, Y. Z. Fan, Z. X. Fan, J. Fang, K. Fang, C. F. Feng, L. Feng, S. H. Feng, Y. L. Feng, B. Gao, C. D. Gao, Q. Gao, W. Gao, M. M. Ge, L. S. Geng, G. H. Gong, Q. B. Gou, M. H. Gu, J. G. Guo, X. L. Guo, Y. Q. Guo, Y. Y. Guo, Y. A. Han, H. H. He, H. N. He, J. C. He, S. L. He, X. B. He, Y. He, M. Heller, Y. K. Hor, C. Hou, X. Hou, H. B. Hu, S. Hu, S. C. Hu, X. J. Hu, D. H. Huang, Q. L. Huang, W. H. Huang, X. T. Huang, Z. C. Huang, F. Ji, X. L. Ji, H. Y. Jia, K. Jiang, Z. J. Jiang, C. Jin, D. Kuleshov, K. Levochkin, B. B. Li, C. Li, C. Li, F. Li, H. B. Li, H. C. Li, H. Y. Li, J. Li, K. Li, W. L. Li, X. Li, X. Li, X. R. Li, Y. Li, Y. Z. Li, Z. Li, Z. Li, E. W. Liang, Y. F. Liang, S. J. Lin, B. Liu, C. Liu, D. Liu, H. Liu, H. D. Liu, J. Liu, J. L. Liu, J. S. Liu, J. Y. Liu, M. Y. Liu, R. Y. Liu, S. M. Liu, W. Liu, Y. N. Liu, Z. X. Liu, W. J. Long, R. Lu, H. K. Lv, B. Q. Ma, L. L. Ma, X. H. Ma, J. R. Mao, A. Masood, W. Mitthumsiri, T. Montaruli, Y. C. Nan, B. Y. Pang, P. Pattarakijwanich, Z. Y. Pei, M. Y. Qi, D. Ruffolo, V. Rulev, A. Sáiz, L. Shao, O. Shchegolev, X. D. Sheng, J. R. Shi, H. C. Song, Y. V. Stenkin, V. Stepanov, Q. N. Sun, X. N. Sun, Z. B. Sun, P. H. T. Tam, Z. B. Tang, W. W. Tian, B. D. Wang, C. Wang, H. Wang, H. G. Wang, J. C. Wang, J. S. Wang, L. P. Wang, L. Y. Wang, R. N. Wang, W. Wang, W. Wang, X. G. Wang, X. J. Wang, X. Y. Wang, Y. D. Wang, Y. J. Wang, Y. P. Wang, Z. Wang, Z. Wang, Z. H. Wang, Z. X. Wang, D. M. Wei, J. J. Wei, Y. J. Wei, T. Wen, C. Y. Wu, H. R. Wu, S. Wu, W. X. Wu, X. F. Wu, S. Q. Xi, J. Xia, J. J. Xia, G. M. Xiang, G. Xiao, H. B. Xiao, G. G. Xin, Y. L. Xin, Y. Xing, D. L. Xu, R. X. Xu, L. Xue, D. H. Yan, C. W. Yang, F. F. Yang, J. Y. Yang, L. L. Yang, M. J. Yang, R. Z. Yang, S. B. Yang, Y. H. Yao, Z. G. Yao, Y. M. Ye, L. Q. Yin, N. Yin, X. H. You, Z. Y. You, Y. H. Yu, Q. Yuan, H. D. Zeng, T. X. Zeng, W. Zeng, Z. K. Zeng, M. Zha, X. X. Zhai, B. B. Zhang, H. M. Zhang, H. Y. Zhang, J. L. Zhang, J. W. Zhang, L. Zhang, L. Zhang, L. X. Zhang, P. F. Zhang, P. P. Zhang, R. Zhang, S. R. Zhang, S. S. Zhang, X. Zhang, X. P. Zhang, Y. Zhang, Y. Zhang, Y. F. Zhang, Y. L. Zhang, B. Zhao, J. Zhao, L. Zhao, L. Z. Zhao, S. P. Zhao, F. Zheng, Y. Zheng, B. Zhou, H. Zhou, J. N. Zhou, P. Zhou, R. Zhou, X. X. Zhou, C. G. Zhu, F. R. Zhu, H. Zhu, K. J. Zhu, X. Zuo, Ultrahigh-energy photons up to 1.4 petaelectronvolts from 12 $\gamma$-ray Galactic sources. *Nature* **594**, 33–36 (2021). doi:10.1038/s41586-021-03498-z Medline
11. Z. Cao, W.-D. Li, C.-L. Liu, Z.-P. Mao, S.-J. Chen, Z.-Y. Deng, K.-L. He, X.-T. Huang, B. Huang, Y.-P. Huang, L.-K. Jia, X.-B. Ji, X.-R. Li, C.-Y. Liu, H.-M. Liu, Q.-M. Ma, X. Ma, J.-F. Qiu, D.-Y. Wang, L.-H. Wu, Z. Wu, Y. Yuan, X.-Y. Zhang, C. Zhao, Y. Zhang, J.-H. Zou, Studies of d*E*/d*x* measurements with the BESIII. *Chinese Phys. C* **34**, 1852 (2010). doi:10.1088/1674-1137/34/12/012
12. H. He, LHAASO Collaboration, Design of the LHAASO detectors. *Radiat. Detect. Technol. Methods* **2**, 7 (2018). doi:10.1007/s41605-018-0037-3
13. Materials and methods are available as supplementary materials.
14. LHAASO Collaboration, Observation of the Crab Nebula with LHAASO-KM2A – a performance study. *Chinese Phys. C* **45**, 025002 (2021). doi:10.1088/1674-1137/abd01b
15. LHAASO Collaboration, Performance of LHAASO-WCDA and Observation of Crab Nebula as a Standard Candle. arXiv:2101.03508 [astro-ph.IM] (2021).
16. LHAASO Collaboration, Construction and On-site Performance of the LHAASO

WFCTA Camera. arXiv:2012.14622 [physics.ins-det] (2020).
17. F. Aharonian, A. G. Akhperjanian, A. R. Bazer-Bachi, M. Beilicke, W. Benbow, D. Berge, K. Bernlöhr, C. Boisson, O. Bolz, V. Borrel, I. Braun, F. Breitling, A. M. Brown, R. Bühler, I. Büsching, S. Carrigan, P. M. Chadwick, L.-M. Chounet, R. Cornils, L. Costamante, B. Degrange, H. J. Dickinson, A. Djannati-Ataï, L. O. C. Drury, G. Dubus, K. Egberts, D. Emmanoulopoulos, P. Espigat, F. Feinstein, E. Ferrero, A. Fiasson, G. Fontaine, S. Funk, S. Funk, Y. A. Gallant, B. Giebels, J. F. Glicenstein, P. Goret, C. Hadjichristidis, D. Hauser, M. Hauser, G. Heinzelmann, G. Henri, G. Hermann, J. A. Hinton, W. Hofmann, M. Holleran, D. Horns, A. Jacholkowska, O. C. de Jager, B. Khélifi, N. Komin, A. Konopelko, K. Kosack, I. J. Latham, R. Le Gallou, A. Lemière, M. Lemoine-Goumard, T. Lohse, J. M. Martin, O. Martineau-Huynh, A. Marcowith, C. Masterson, T. J. L. McComb, M. de Naurois, D. Nedbal, S. J. Nolan, A. Noutsos, K. J. Orford, J. L. Osborne, M. Ouchrif, M. Panter, G. Pelletier, S. Pita, G. Pühlhofer, M. Punch, B. C. Raubenheimer, M. Raue, S. M. Rayner, A. Reimer, O. Reimer, J. Ripken, L. Rob, L. Rolland, G. Rowell, V. Sahakian, L. Saugé, S. Schlenker, R. Schlickeiser, U. Schwanke, H. Sol, D. Spangler, F. Spanier, R. Steenkamp, C. Stegmann, G. Superina, J.-P. Tavernet, R. Terrier, C. G. Théoret, M. Tluczykont, C. van Eldik, G. Vasileiadis, C. Venter, P. Vincent, H. J. Völk, S. J. Wagner, M. Ward, Observations of the Crab nebula with HESS. *Astron. Astrophys.* **457**, 899–915 (2006). doi:10.1051/0004-6361:20065351
18. K. Meagher, VERITAS Collaboration, *34th International Cosmic Ray Conference (ICRC2015)* (2015), vol. 34 of *International Cosmic Ray Conference*, p. 792.
19. B. Bartoli, P. Bernardini, X. J. Bi, P. Branchini, A. Budano, P. Camarri, Z. Cao, R. Cardarelli, S. Catalanotti, S. Z. Chen, T. L. Chen, P. Creti, S. W. Cui, B. Z. Dai, A. D'Amone, Danzengluobu, I. De Mitri, B. D'Ettorre Piazzoli, T. Di Girolamo, G. Di Sciascio, C. F. Feng, Z. Feng, Z. Feng, Q. B. Gou, Y. Q. Guo, H. H. He, H. Hu, H. Hu, M. Iacovacci, R. Iuppa, H. Y. Jia, Labaciren, H. J. Li, G. Liguori, C. Liu, J. Liu, M. Y. Liu, H. Lu, L. L. Ma, X. H. Ma, G. Mancarella, S. M. Mari, G. Marsella, D. Martello, S. Mastroianni, P. Montini, C. C. Ning, M. Panareo, L. Perrone, P. Pistilli, F. Ruggieri, P. Salvini, R. Santonico, P. R. Shen, X. D. Sheng, F. Shi, A. Surdo, Y. H. Tan, P. Vallania, S. Vernetto, C. Vigorito, H. Wang, C. Y. Wu, H. R. Wu, L. Xue, Q. Y. Yang, X. C. Yang, Z. G. Yao, A. F. Yuan, M. Zha, H. M. Zhang, L. Zhang, X. Y. Zhang, Y. Zhang, J. Zhao, Zhaxiciren, Zhaxisangzhu, X. X. Zhou, F. R. Zhu, Q. Q. Zhu, G. Zizzi, E. Striani, Crab Nebula: Five-year observation with ARGO-YBJ. *Astrophys. J.* **798**, 119 (2015). doi:10.1088/0004-637X/798/2/119
20. S. Ansoldi, L. A. Antonelli, P. Antoranz, A. Babic, P. Bangale, U. Barres de Almeida, J. A. Barrio, J. Becerra González, W. Bednarek, E. Bernardini, B. Biasuzzi, A. Biland, O. Blanch, S. Bonnefoy, G. Bonnoli, F. Borracci, T. Bretz, E. Carmona, A. Carosi, P. Colin, E. Colombo, J. L. Contreras, J. Cortina, S. Covino, P. Da Vela, F. Dazzi, A. De Angelis, G. De Caneva, B. De Lotto, E. de Oña Wilhelmi, C. Delgado Mendez, F. Di Pierro, D. Dominis Prester, D. Dorner, M. Doro, S. Einecke, D. Eisenacher Glawion, D. Elsaesser, A. Fernández-Barral, D. Fidalgo, M. V. Fonseca, L. Font, K. Frantzen, C. Fruck, D. Galindo, R. J. García López, M. Garczarczyk, D. Garrido Terrats, M. Gaug, N. Godinović, A. González Muñoz, S. R. Gozzini, Y. Hanabata, M. Hayashida, J. Herrera, K. Hirotani, J. Hose, D. Hrupec, G. Hughes, W. Idec, H. Kellermann, M. L. Knoetig, K. Kodani, Y. Konno, J. Krause, H. Kubo, J. Kushida, A. La Barbera, D. Lelas, N. Lewandowska, E. Lindfors, S. Lombardi, F. Longo, M. López, R. López-Coto, A. López-Oramas, E. Lorenz, M. Makariev, K. Mallot, G. Maneva, K. Mannheim, L. Maraschi, B. Marcote, M. Mariotti, M. Martínez, D. Mazin, U. Menzel, J. M. Miranda, R. Mirzoyan, A. Moralejo, P. Munar-Adrover, D. Nakajima, V. Neustroev, A. Niedzwiecki, M. Nevas Rosillo, K. Nilsson, K. Nishijima, K. Noda, R. Orito, A. Overkemping, S. Paiano, M. Palatiello, D. Paneque, R. Paoletti, J. M. Paredes, X. Paredes-Fortuny, M. Persic, J. Poutanen, P. G. Prada Moroni, E. Prandini, I. Puljak, R. Reinthal, W. Rhode, M. Ribó, J. Rico, J. Rodriguez Garcia, T. Saito, K. Saito, K. Satalecka, V. Scalzotto, V. Scapin, C. Schultz, T. Schweizer, S. N. Shore, A. Sillanpää, J. Sitarek, I. Snidaric, D. Sobczynska, A. Stamerra, T. Steinbring, M. Strzys, L. Takalo, H. Takami, F. Tavecchio, P. Temnikov, T. Terzić, D. Tescaro, M. Teshima, J. Thaele, D. F. Torres, T. Toyama, A. Treves, J. Ward, M. Will, R. Zanin, Teraelectronvolt pulsed emission from the Crab Pulsar detected by MAGIC. *Astron. Astrophys.* **585**, A133 (2016). doi:10.1051/0004-6361/201526853
21. F. A. Aharonian, S. V. Bogovalov, D. Khangulyan, Abrupt acceleration of a 'cold' ultrarelativistic wind from the Crab pulsar. *Nature* **482**, 507–509 (2012). doi:10.1038/nature10793 Medline
22. I. Mochol, J. Petri, Very high energy emission as a probe of relativistic magnetic reconnection in pulsar winds. *Mon. Not. R. Astron. Soc.* **449**, L51–L55 (2015). doi:10.1093/mnrasl/slv018
23. P. K. H. Yeung, Inferring the origins of the pulsed $\gamma$-ray emission from the Crab pulsar with ten-year *Fermi*-LAT data. *Astron. Astrophys.* **640**, A43 (2020). doi:10.1051/0004-6361/202038166
24. O. C. de Jager, A. K. Harding, The expected high-energy to ultra-high-energy gamma-ray spectrum of the Crab Nebula. *Astrophys. J.* **396**, 161 (1992). doi:10.1086/171706
25. A. M. Atoyan, F. A. Aharonian, On the mechanisms of gamma radiation in the Crab Nebula. *Mon. Not. R. Astron. Soc.* **278**, 525–541 (1996). doi:10.1093/mnras/278.2.525
26. M. J. Rees, J. E. Gunn, The Origin of the Magnetic Field and Relativistic Particles in the Crab Nebula. *Mon. Not. R. Astron. Soc.* **167**, 1–12 (1974). doi:10.1093/mnras/167.1.1
27. C. F. Kennel, F. V. Coroniti, Confinement of the Crab pulsar's wind by its supernova remnant. *Astrophys. J.* **283**, 694 (1984). doi:10.1086/162356
28. M. Meyer, D. Horns, H. S. Zechlin, The Crab Nebula as a standard candle in very high-energy astrophysics. *Astron. Astrophys.* **523**, A2 (2010). doi:10.1051/0004-6361/201014108
29. L. Kuiper, W. Hermsen, G. Cusumano, R. Diehl, V. Schönfelder, A. Strong, K. Bennett, M. L. McConnell, The Crab pulsar in the 0.75-30 MeV range as seen by CGRO COMPTEL. *Astron. Astrophys.* **378**, 918–935 (2001). doi:10.1051/0004-6361:20011256
30. M. C. Weisskopf, J. J. Hester, A. F. Tennant, R. F. Elsner, N. S. Schulz, H. L. Marshall, M. Karovska, J. S. Nichols, D. A. Swartz, J. J. Kolodziejczak, S. L. O'Dell, Discovery of Spatial and Spectral Structure in the X-Ray Emission from the Crab Nebula. *Astrophys. J.* **536**, L81–L84 (2000). doi:10.1086/312733 Medline
31. M. Tavani, A. Bulgarelli, V. Vittorini, A. Pellizzoni, E. Striani, P. Caraveo, M. C. Weisskopf, A. Tennant, G. Pucella, A. Trois, E. Costa, Y. Evangelista, C. Pittori, F. Verrecchia, E. Del Monte, R. Campana, M. Pilia, A. De Luca, I. Donnarumma, D. Horns, C. Ferrigno, C. O. Heinke, M. Trifoglio, F. Gianotti, S. Vercellone, A. Argan, G. Barbiellini, P. W. Cattaneo, A. W. Chen, T. Contessi, F. D'Ammando, G. DePris, G. Di Cocco, G. Di Persio, M. Feroci, A. Ferrari, M. Galli, A. Giuliani, M. Giusti, C. Labanti, I. Lapshov, F. Lazzarotto, P. Lipari, F. Longo, F. Fuschino, M. Marisaldi, S. Mereghetti, E. Morelli, E. Moretti, A. Morselli, L. Pacciani, F. Perotti, G. Piano, P. Picozza, M. Prest, M. Rapisarda, A. Rappoldi, A. Rubini, S. Sabatini, P. Soffitta, E. Vallazza, A. Zambra, D. Zanello, F. Lucarelli, P. Santolamazza, P. Giommi, L. Salotti, G. F. Bignami, Discovery of powerful gamma-ray flares from the Crab Nebula. *Science* **331**, 736–739 (2011). doi:10.1126/science.1200083 Medline
32. R. Bühler, R. Blandford, The surprising Crab pulsar and its nebula: A review. *Rep. Prog. Phys.* **77**, 066901 (2014). doi:10.1088/0034-4885/77/6/066901 Medline
33. F. A. Aharonian, A. A. Belyanin, E. V. Derishev, V. V. Kocharovsky, V. V. Kocharovsky, Constraints on the extremely high-energy cosmic ray accelerators from classical electrodynamics. *Phys. Rev. D* **66**, 023005 (2002). doi:10.1103/PhysRevD.66.023005
34. M. A. Malkov, L. O. Drury, Nonlinear theory of diffusive acceleration of particles by shock waves. *Rep. Prog. Phys.* **64**, 429–481 (2001). doi:10.1088/0034-4885/64/4/201
35. D. L. Kaplan, S. Chatterjee, B. M. Gaensler, J. Anderson, A Precise Proper Motion for the Crab Pulsar, and the Difficulty of Testing Spin-Kick Alignment for Young Neutron Stars. *Astrophys. J.* **677**, 1201–1215 (2008). doi:10.1086/529026
36. D. Khangulyan, F. A. Aharonian, S. R. Kelner, Simple analytical approximations for treatment of inverse Compton scattering of relativistic electrons in the blackbody radiation field. *Astrophys. J.* **783**, 100 (2014). doi:10.1088/0004-637X/783/2/100
37. O. C. de Jager, A. K. Harding, P. F. Michelson, H. I. Nel, P. L. Nolan, P. Sreekumar, D. J. Thompson, Gamma-Ray Observations of the Crab Nebula: A Study of the Synchro-Compton Spectrum. *Astrophys. J.* **457**, 253 (1996). doi:10.1086/176726
38. D. Volpi, L. Del Zanna, E. Amato, N. Bucciantini, Non-thermal emission from relativistic MHD simulations of pulsar wind nebulae: From synchrotron to inverse Compton. *Astron. Astrophys.* **485**, 337–349 (2008). doi:10.1051/0004-6361:200809424
39. D. Khangulyan, M. Arakawa, F. Aharonian, Detection of ultra-high-energy gamma rays from the Crab Nebula: Physical implications. *Mon. Not. R. Astron. Soc.* **491**, 3217–3224 (2020). doi:10.1093/mnras/stz3261

40. D. Volpi, L. Del Zanna, E. Amato, N. Bucciantini, Non-thermal emission from relativistic MHD simulations of pulsar wind nebulae: From synchrotron to inverse Compton. *Astron. Astrophys.* **485**, 337–349 (2008). doi:10.1051/0004-6361:200809424
41. N. Bucciantini, J. Arons, E. Amato, Modelling spectral evolution of pulsar wind nebulae inside supernova remnants. *Mon. Not. R. Astron. Soc.* **410**, 381–398 (2011). doi:10.1111/j.1365-2966.2010.17449.x
42. J. Arons, Magnetars in the Metagalaxy: An Origin for Ultra–High-Energy Cosmic Rays in the Nearby Universe. *Astrophys. J.* **589**, 871–892 (2003). doi:10.1086/374776
43. LHAASO Collaboration, Calibration of the Air Shower Energy Scale of the Water and Air Cherenkov Techniques in the LHAASO experiment. arXiv:2104.04965 [astro-ph.IM] (2021).
44. P. K. F. Grieder, *Extensive Air Showers: High Energy Phenomena and Astrophysical Aspects - A Tutorial, Reference Manual and Data Book* (Springer, 2010).
45. E. Derishev, F. Aharonian, Exact Analytical Expression for the Synchrotron Radiation Spectrum in the Gaussian Turbulent Magnetic Field. *Astrophys. J.* **887**, 181 (2019). doi:10.3847/1538-4357/ab536a
46. C. C. Popescu, R. Yang, R. J. Tuffs, G. Natale, M. Rushton, F. Aharonian, A radiation transfer model for the Milky Way: I. Radiation fields and application to high-energy astrophysics. *Mon. Not. R. Astron. Soc.* **470**, 2539–2558 (2017). doi:10.1093/mnras/stx1282
47. M. Lyutikov, T. Temim, S. Komissarov, P. Slane, L. Sironi, L. Comisso, Interpreting Crab Nebula's synchrotron spectrum: Two acceleration mechanisms. *Mon. Not. R. Astron. Soc.* **489**, 2403–2416 (2019). doi:10.1093/mnras/stz2023
48. L. Sironi, A. Spitkovsky, J. Arons, The maximum energy of accelerated particles in relativistic collisionless shocks. *Astrophys. J.* **771**, 54 (2013). doi:10.1088/0004-637X/771/1/54
49. L. Sironi, A. Spitkovsky, Relativistic reconnection: An efficient source of non-thermal particles. *Astrophys. J.* **783**, L21 (2014). doi:10.1088/2041-8205/783/1/L21
50. X. Zhang, Y. Chen, J. Huang, D. Chen, Modelling the broadest spectral band of the Crab nebula and constraining the ion acceleration efficiency. *Mon. Not. R. Astron. Soc.* **497**, 3477–3483 (2020). doi:10.1093/mnras/staa2151
51. P. Blasi, R. I. Epstein, A. V. Olinto, Ultra-High-Energy Cosmic Rays from Young Neutron Star Winds. *Astrophys. J.* **533**, L123–L126 (2000). doi:10.1086/312626 Medline
52. C. Guépin, B. Cerutti, K. Kotera, Proton acceleration in pulsar magnetospheres. *Astron. Astrophys.* **635**, A138 (2020). doi:10.1051/0004-6361/201936816
53. M. Lemoine, K. Kotera, J. Pétri, On ultra-high energy cosmic ray acceleration at the termination shock of young pulsar winds. *J. Cosmol. Astropart. Phys.* **2015**, 016 (2015). doi:10.1088/1475-7516/2015/07/016
54. E. Amato, D. Guetta, P. Blasi, Signatures of high energy protons in pulsar winds. *Astron. Astrophys.* **402**, 827–836 (2003). doi:10.1051/0004-6361:20030279
55. J. Arons, Filamentation instability of interacting current sheets in striped relativistic winds: The origin of low sigma? *Int. J. Mod. Phys. D* **17**, 1419–1430 (2008). doi:10.1142/S0218271808012991
56. P. J. Owen, M. J. Barlow, The dust and gas content of the Crab Nebula. *Astrophys. J.* **801**, 141 (2015). doi:10.1088/0004-637X/801/2/141
57. E. Kafexhiu, F. Aharonian, A. M. Taylor, G. S. Vila, Parametrization of gamma-ray production cross sections for *pp* interactions in a broad proton energy range from the kinematic threshold to PeV energies. *Phys. Rev. D* **90**, 123014 (2014). doi:10.1103/PhysRevD.90.123014
58. J. E. Baldwin, *The Crab Nebula*, R. D. Davies, F. Graham-Smith, eds. (1971), vol. 46 of *IAU Symposium*, p. 22.
59. J. F. Macías-Pérez, F. Mayet, J. Aumont, F.-X. Désert, Global spectral energy distribution of the Crab Nebula in the prospect of the *Planck* satellite polarization calibration. *Astrophys. J.* **711**, 417–423 (2010). doi:10.1088/0004-637X/711/1/417
60. E. P. Ney, W. A. Stein, Observations of the Crab Nebula at $\lambda$ = 5800 Å 2.2 μ, and 3.5 μ with a 4-MINUTE Beam. *Astrophys. J.* **152**, L21 (1968). doi:10.1086/180170
61. G. L. Grasdalen, Near infrared observations of the Crab nebula. *Publ. Astron. Soc. Pac.* **91**, 436 (1979). doi:10.1086/130516
62. D. A. Green, R. J. Tuffs, C. C. Popescu, Far-infrared and submillimetre observations of the Crab nebula. *Mon. Not. R. Astron. Soc.* **355**, 1315–1326 (2004). doi:10.1111/j.1365-2966.2004.08414.x
63. T. Temim, R. D. Gehrz, C. E. Woodward, T. L. Roellig, N. Smith, L. Rudnick, E. F. Polomski, K. Davidson, L. Yuen, T. Onaka, *Spitzer Space Telescope* Infrared Imaging and Spectroscopy of the Crab Nebula. *Astron. J.* **132**, 1610–1623 (2006). doi:10.1086/507076
64. M. P. Véron-Cetty, L. Woltjer, Spectrophotometry of the continuum in the Crab Nebula. *Astron. Astrophys.* **270**, 370–378 (1993).
65. G. S. Hennessy, R. W. O'Connell, K. P. Cheng, R. C. Bohlin, N. R. Collins, T. R. Gull, P. Hintzen, J. E. Isensee, W. B. Landsman, M. S. Roberts, A. M. Smith, E. P. Smith, T. P. Stecher, Ultraviolet Imaging Telescope observations of the Crab Nebula. *Astrophys. J.* **395**, L13 (1992). doi:10.1086/186477

## ACKNOWLEDGMENTS

We thank all staff members who work at the LHAASO site above 4400 m above the sea level year-round to maintain the detector and keep the electricity power supply and other components of the experiment operating smoothly. **Funding**: This work was supported in China by the National Key R&D program of China under grants 2018YFA0404201, 2018YFA0404202, 2018YFA0404203, 2018YFA0404204, by NSFC under grants No.12022502, No.11905227, No.U1831208, No.U1931112, No.11635011, No.11761141001, No.11905240, No.11675204, No.11475190, No.U2031105, No.U1831129; and in Thailand by grant RTA6280002 from Thailand Science Research and Innovation. Chengdu Management Committee of Tianfu New Area provided financial support for research with LHAASO data. **Author contributions:** Z.Cao and F.Aharonian led drafting of the text about the experiment and interpretation, respectively. S.Z.Chen led the KM2A data analysis with the team members C.Li and L.Y.Wang and others. LYW carried out event-by-event analysis and corresponding simulation. S.J.Lin and M.Zha led teams to conduct the spectrum analysis using WCDA data and corresponding cross checking. S.S.Zhang led the WFCTA team including L.Q.Yin to perform the combined analysis of all data from WFCTA, WCDA and KM2A for commonly registered events. LQY carried out the specific multi-component analysis and corresponding simulation. F.Aharonian and R.Y.Liu conducted the theoretical interpretation. RYL produced all corresponding calculations, all figures, and edited the manuscript. ZC is the spokesperson of LHAASO Collaboration, PI of the LHAASO project in China, and led the specific working group for this paper involving all corresponding authors. The Editorial Board of the LHAASO Collaboration was led by S.M.Liu and D.della Volpe, who organized internal review before submission. B.D'Ettorre Piazzoli participated in manuscript revision and corresponding discussion. All other authors participated in data analysis, including event reconstruction, simulation and event building with multi components, detector calibration, operation and maintenance of all scintillator counters, muon detectors, water ponds and Cherenkov telescopes. The detector arrays were still under construction while the data were taken for this paper. Many authors participated in the detector construction and deployment. **Competing interests:** There are no conflict of interests to declare for any collaboration members. **Data and materials availability:** Data and software to reproduce these results are available on the LHAASO public data web page at http://english.ihep.cas.cn/doc/4035.html, including the event list, results of the background rate calculations, numerical values of the derived WCDA and KM2A spectra (Fig. 3) and SED (Fig. 4), and the code used to produce the SED and significance maps (fig. S1). The software we wrote for simulation of the detectors and background rate calculations is restricted by the terms of a grant from China's National Commission of Development and Reform, due to legal restrictions imposed during the construction phase of LHAASO. Readers who are willing to become associated members of the LHAASO Collaboration can request a copy under the condition that any resulting paper is authored by all collaboration members, including associated members. Interested readers should contact the corresponding authors for details.

## SUPPLEMENTARY MATERIALS

science.sciencemag.org/cgi/content/full/science.abg5137/DC1
LHAASO Collaboration Author List
Materials and Methods
Supplementary Text

Figs. S1 to S9
Tables S1 and S2
References (*43*–*65*)

12 January 2021; accepted 23 June 2021
Published online 8 July 2021
10.1126/science.abg5137

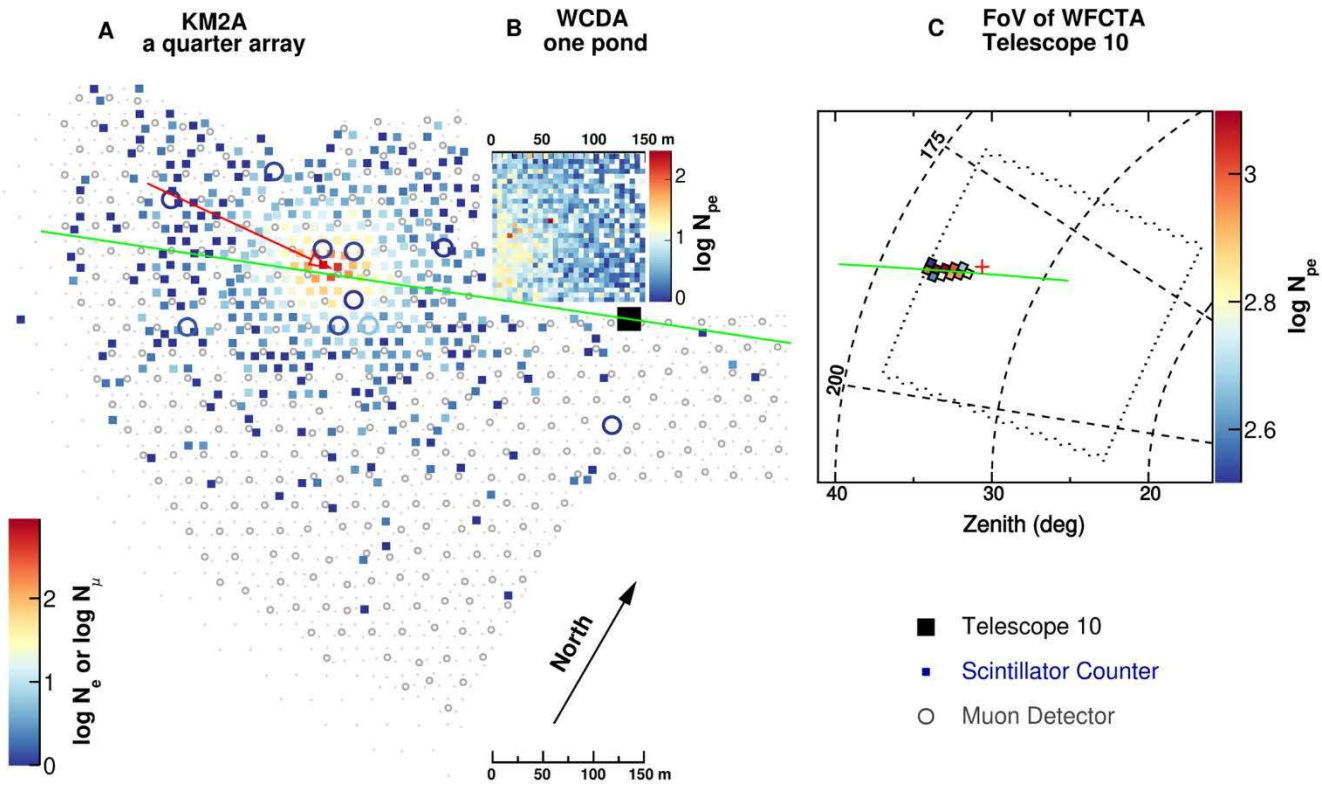


**Fig. 1. The 0.88 PeV γ-ray event from the Crab recorded by the LHAASO detectors.** In panel A, squares indicate the scintillator counters of KM2A, colored according to the logarithm of number of detected particles $N_e$ (color bar). The open circles indicate the 11 Muon Detectors of KM2A triggered by the shower. The position of the core is indicated by the red arrow, which is orientated in the arrival direction of the primary photon. Panel B shows the map of WCDA detector units. The logarithm of the number of photoelectrons recorded in each unit is indicated by the color. The scale is represented by the color bar. On the southern side of WCDA is located Telescope-10 of WFCTA (black square) which also detected the event. Panel C shows the telescope FoV outlined by the dotted lines, while the dashed arcs indicate zenith angles of 20°, 30°, 40°, from right to left and dashed lines indicate azimuth angles of 175°, 200° counterclockwise. The shower image, composed of 11 pixels, started about 34° in zenith and stretched to the edge of the FoV at 38°. The color scale shows the logarithm of the number of photoelectrons in each pixel. The main axis of the image in the FoV of the telescope indicates the shower-telescope-plane which is consistent with the event direction (indicated by the red cross in panel C) reconstructed using KM2A. The green line in panel A is the intersection of the shower plane and the ground, which is consistent with the shower core.

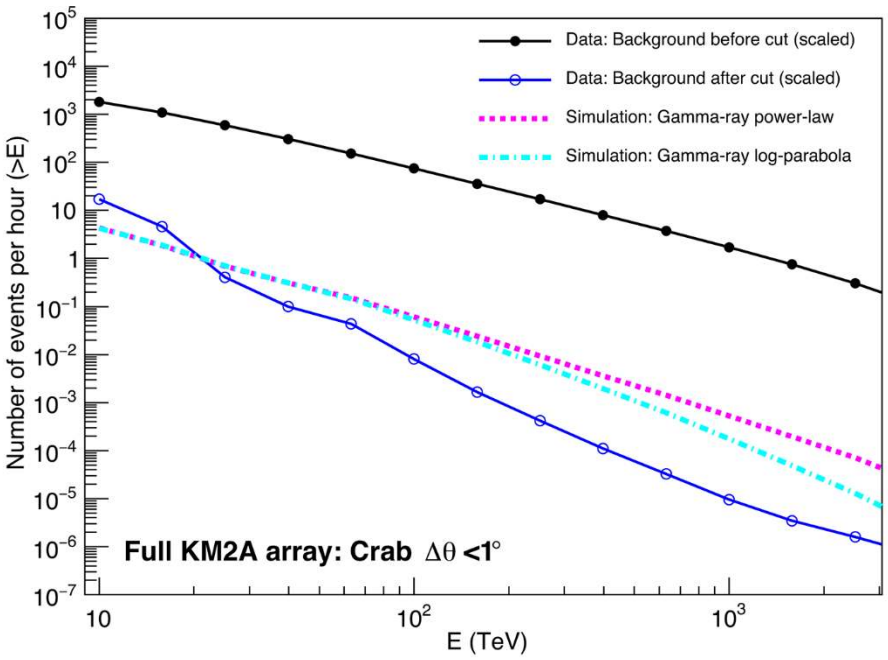


**Fig. 2. The rates of detection of γ-rays from the Crab and the cosmic ray background events above the shower energy *E* by the 1 km² array in a cone of 1° centered at the Crab direction.** The rates correspond to the number of events per hour of observation of the source within the FoV of KM2A. *E* is the reconstructed shower energy. The cyan dash-dotted and pink dashed lines represent the integrated detection rates of γ-rays from the Crab, based on log-parabola and power-law models fitted to the measured fluxes (see Fig. 3), respectively. The black filled circles show the rate of cosmic ray events accumulated by KM2A. The integrated rate can be approximately described as power law with index of -1.6. The blue open circles represent the integrated rate of cosmic ray events after the 'muon cut' filter.

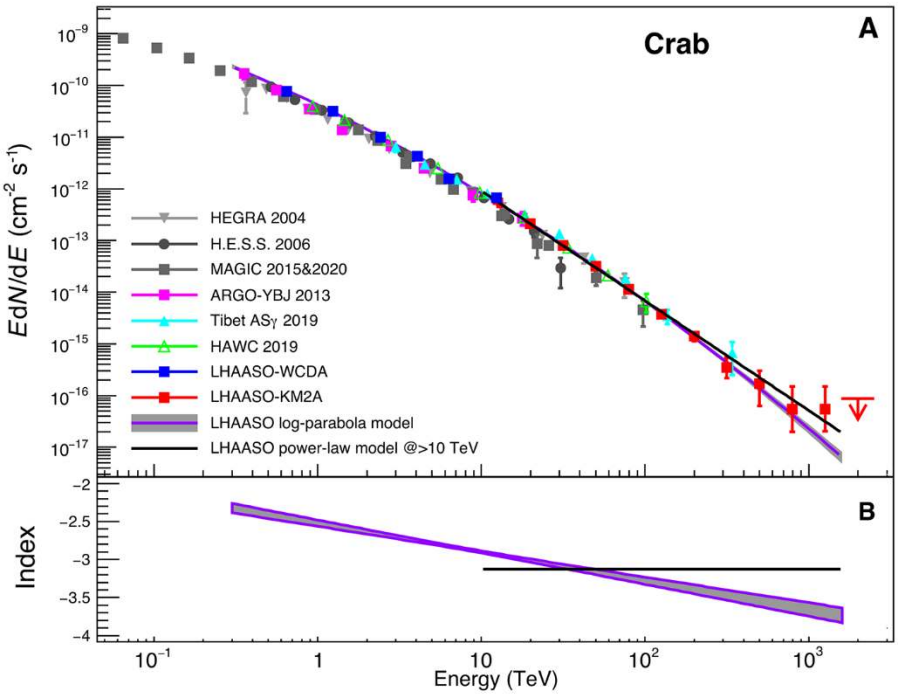


**Fig. 3. γ-ray flux of the Crab measured by LHAASO and spectral fitting.** Panel A shows TeV to PeV γ-ray fluxes of the Crab plotted as *E*d*N*/d*E*. The red squares and blue squares are the spectral points measured using KM2A and WCDA, respectively. The spectral points above 100 TeV were obtained in the signal-dominated regime, with 89 detected γ-rays and 2 events expected from CR induced (hadronic) air showers after the muon cuts. No events were detected in the 1.6 to 2.5 PeV bin where an arrow indicates the flux upper limit at 90% confidence level. The purple line shows the fitting using a log-parabola (LP) model in the 0.3 TeV to 1.6 PeV interval ($\chi^2$ / *dof*: 9.3/14). For comparison, the black line shows the fitting using a simpler power-law (PL) model in the 10 TeV to 1.6 PeV interval ($\chi^2$ / *dof*: 5.4/9). Also plotted are previous observations of the Crab by other facilities: High Energy Gamma Ray Astronomy (*5*), High Energy Stereoscopic System (*17*), Major Atmospheric Gamma Imaging Cherenkov Telescope (*4*, *6*), Astrophysical Radiation by Ground-based Observation at Yang Ba Jing (*19*), High Altitude Water Cherenkov Detector (*7*), Tibet Air Shower array (*8*). Panel B shows the energy-dependent local power-law index Γ derived by the log-parabola model fitting, as indicated by the purple band. For comparison, the black line shows the photon index 3.12 ± 0.03 derived from the simpler power-law model fitting. Error bars represent one standard deviation.

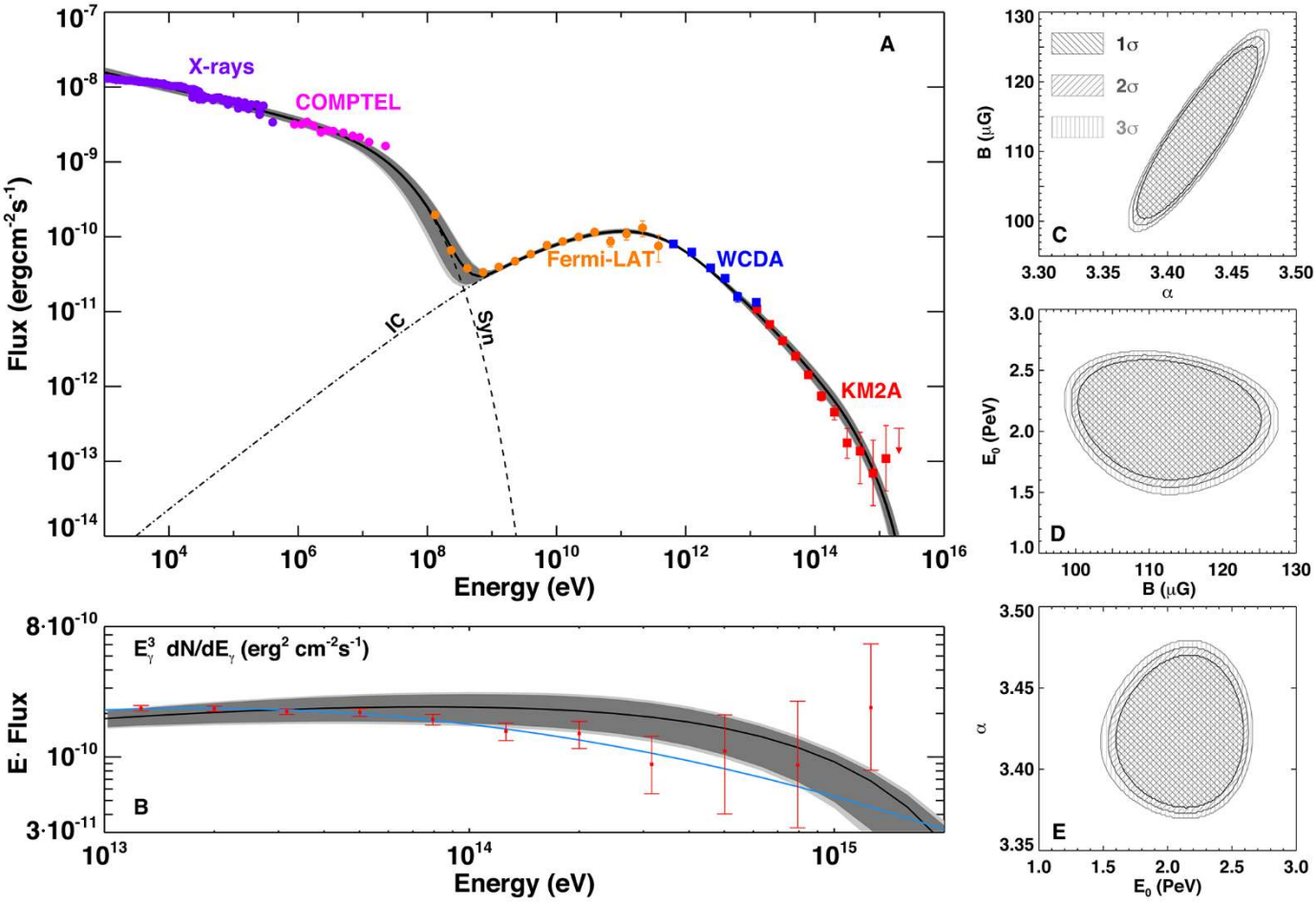


**Fig. 4. The Spectral Energy Distribution of the Crab Nebula.** Panel A: The black curves represent the fluxes of the synchrotron and IC components of radiation of an electron population calculated within the one-zone model. The electron spectrum above 1 TeV is assumed to be a power-law function terminated by a super-exponential cutoff, $E^{-\alpha}\ \exp[-(E\ /\ E_0)^2]$. The best fitting model parameters are: $\alpha = 3.42 \pm 0.05$, $E_0 = 2.15^{+0.55}_{-0.65}$ PeV, $B = 112^{+15}_{-13}$ μG. The total energy in electrons above 1 TeV is $W_e = 7.7 \times 10^{47}$ erg. A break in the electron spectrum at $E_b = 0.76$ TeV is assumed to provide a consistency with the GeV γ-ray and low-frequency synchrotron data (see supplementary text and fig. S6). The dark-grey and light-grey shaded regions show the 1σ and 3σ uncertainty regions, respectively. The purple and the magenta circles show the X-ray and the MeV emission of the Crab Nebula (*29*). The orange circles represent the Crab observations by Fermi-Large Area Telescope (LAT) in the non-flare state (*3*). The blue and red squares represent WCDA and KM2A measurements reported in this work. Panel B zooms into the fluxes above 10 TeV, plotted as $E^3 dN/dE$. The blue curve presents the log-parabola spectral fitting shown in in Fig. 3. Panel C, D and E show the 2-dimensional projected parameter spaces of the free parameters α, $B$ and $E_0$, with uncertainty regions indicated by the hatching shown in the legend.